RESEARCH ARTICLE | DECEMBER 01 2025

Peculiarities of the mechanism of subnanosecond switching of high-voltage pulses in eptron

P. A. Bokhan ; P. P. Gugin ; M. A. Lavrukhin ; D. E. Zakrevsky ; I. V. Schweigert

Phys. Plasmas 32, 123501 (2025)
https://doi.org/10.1063/5.0289661

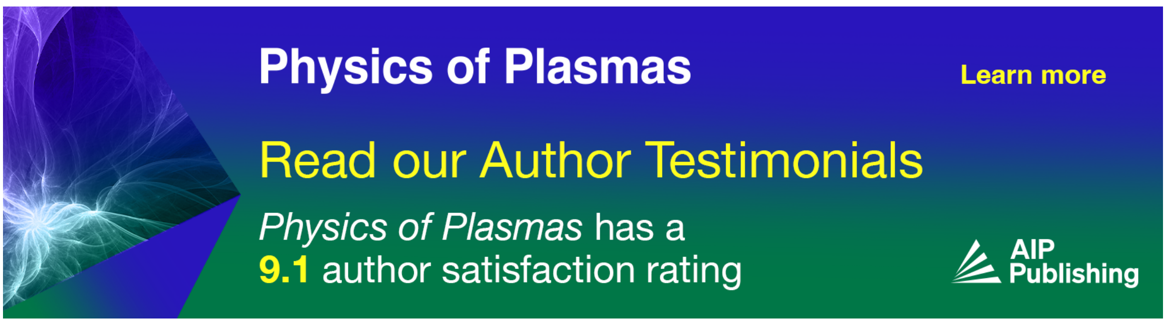

Physics of Plasmas ARTICLE pubs.aip.org/aip/pop

Peculiarities of the mechanism of subnanosecond switching of high-voltage pulses in eptron

Cite as: Phys. Plasmas **32**, 123501 (2025); doi: 10.1063/5.0289661
Submitted: 9 July 2025 · Accepted: 9 November 2025 ·
Published Online: 1 December 2025

P. A. Bokhan,[1] P. P. Gugin,[1] M. A. Lavrukhin,[1] D. E. Zakrevsky,[1,2,a)] and I. V. Schweigert[1]

AFFILIATIONS

[1]Rzhanov Institute of Semiconductor Physics SB RAS, Novosibirsk 630090, Russia
[2]Novosibirsk State Technical University, Novosibirsk 630073, Russia

[a)]Author to whom correspondence should be addressed: zakrdm@isp.nsc.ru

ABSTRACT

The initial stage of breakdown in a switching device based on capillary discharge with plasma cathode (eptron) has been investigated. The discharge in the switch develops in two stages due to different mechanisms of plasma creation in the capillary and plasma cathode, which leads to the reflection of the ionization wave from the weakly ionized plasma of the cathode. Increasing its concentration by means of pulse repetition rate, initiating pulse energy, and gas pressure variation suppresses voltage fluctuations on the load and brings both discharge stages closer, enabling subnanosecond switching times.

I. INTRODUCTION

In recent years, methods of generation of high-voltage pulses with subnanosecond and picosecond leading edge duration, including high repetition rate devices, have been intensively developed. Their realization is based both on the improvement of traditional switches using gas, mainly spark discharges,[1–6] and on the development of various types of semiconductor devices.[7–10] The first group includes plasma switching devices (eptrons) based on the development of current in a capillary discharge with a plasma cathode with various methods of plasma creation inside it.[11–13] Their advantage, as well as some other systems based on semiconductor devices,[10] provides pulse power generators the opportunity to operate at voltages of tens of kilovolts and pulse repetition rates of tens to hundreds of kilohertz. The application of such generators refines frequency-energy characteristics of lasers on self-terminating transitions[12,14] and allows us to obtain a stable volumetric current flow of atmospheric pressure discharge with high energy input.[13]

The peculiarity of the eptron, which is a consequence of the use of two types of discharge in one device, is the two-stage breakdown operation mode.[12] At the first stage, the breakdown in the capillary channel is realized due to the development of discharge on the capacitive components of the device. At the second stage, the main current growth is realized due to secondary processes of electron emission from the cold cathode or by the formation of high-density plasma in it. Usually, the switching time at both stages is less than 1 ns, but the delay time of the second stage relative to the first stage is in units of nanoseconds. This reduces the switching efficiency in this time interval up to 70%–80% and is accompanied by rapid fluctuations of both the voltage pulse, even on the Ohmic load, and the current through it. This undesirable phenomenon stimulates the need for a detailed study of the initial stages of breakdown with subnanosecond resolution time, which is the purpose of the present work.

II. EXPERIMENTAL SETUP

The experimental study of the initial stage of breakdown was carried out with a capillary structure made of Al_2O_3 ceramics with a length of 50 mm and a cross section of 1×15 mm (Fig. 1). To prevent the generation of runaway electrons and consequently increase the delay of discharge development, a square-wave type capillary channel with a length of 6 mm sections was used. The experiments were carried out with two types of cathodes. The first one was made of silicon carbide SiC ceramics with length $l = 24$ mm and inner diameter $d = 28$ mm (inner volume, 15 cm^3), Fig. 1(a). The second variant was a stainless-steel cathode with $l = 11$ mm and $d = 13$ mm (inner volume, 1.5 cm^3), Fig. 1(b). The sides of both cathodes were closed by glass plates with a thickness of 4 mm. A rectangular hole with a cross section of 20×3 mm was milled in the plate adjacent to the capillary channel, through which the discharge from the capillary reached the cathode. On the other side of the cathode, an electrical input was inserted to organize the preionization discharge in the hollow cathode assembly.

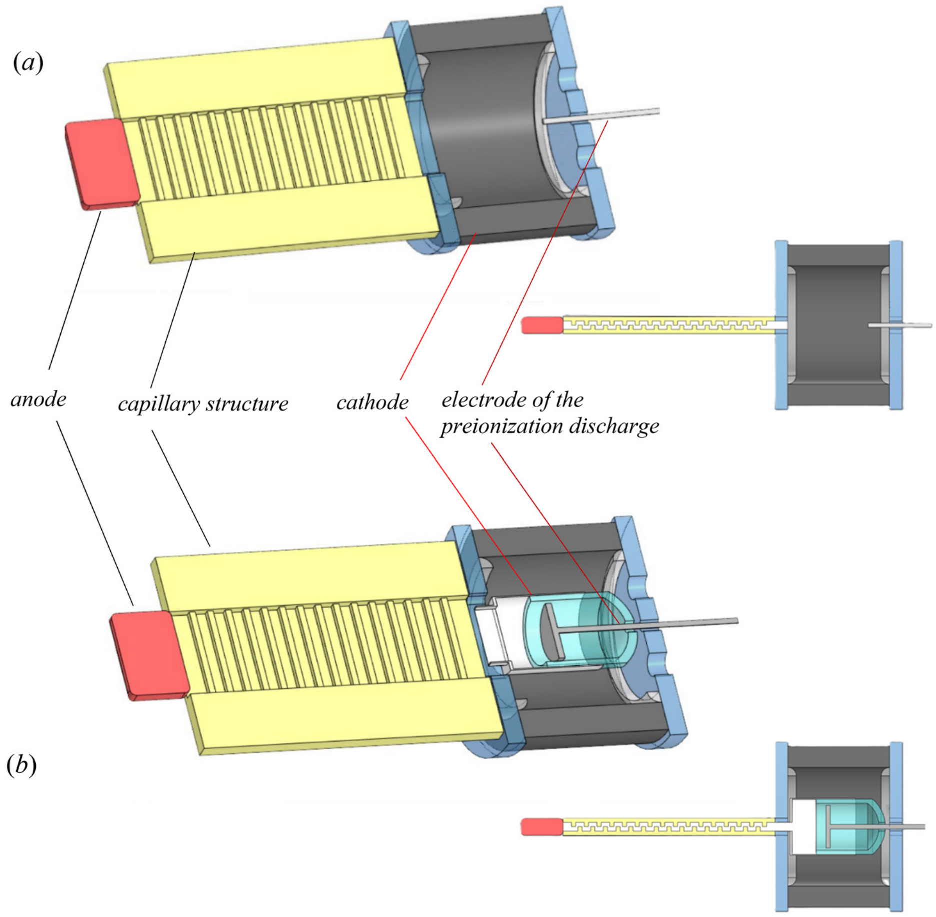

FIG. 1. Eptron designs based on slit capillary discharges with plasma cathode: (a) Cell with a *SiC* cathode; and (b) Cell with a stainless-steel cathode.

Two variants for generating the initiating pulses were used. In the first case, parameters of preionization pulses were the same for both cathodes and were realized by discharging capacitance $C_{pre} = 500$ pF, preliminary charged to voltage $U_{Cpre} = 5$ kV during ∼100 ns. The initiating pulses were applied with an adjustable delay relative to the voltage pulse on the anode of the eptron.

The calculated concentration of plasma in the cathode cavity achieved with such preionization pulses is $n_{e0} \approx 5 \times 10^{13}$ cm^{-3} for the cell with a *SiC* cathode and $n_{e0} \approx 5 \times 10^{14}$ sm^{-3} for the cell with a stainless steel cathode. The charge concentration in the plasma could be varied by installing ballast resistors $R_b = 0$–$300\ \Omega$ in the discharge circuit. In some cases, enhanced preionization with voltage on C_{pre} up to $U_{Cpre} = 10$ kV was used. A detailed description of the electrical circuit of discharge cell excitation is given in Ref. 13.

In the second case, the initiating pulse was automatically synchronized with the main pulse applied to the eptron by generating it using the circuit shown in Fig. 2. The operating voltage was generated by discharging capacitance $C_1 = 2\ \mu$F through a set of 8 IRG4PH50U transistors. The voltage of the generated pulse with a duration of $\sim 1\ \mu$s and an amplitude up to 800 V was increased by a transformer up to 30 kV and then compressed by a two-stage magnetic line so that the operating capacitance $C_2 = 500$ pF was charged by a positive pulse during the time ∼150 ns. Figure 3 shows the voltage oscillograms at the eptron and across the Ohmic load $R_L = 200\ \Omega$ for the 1st, 2nd, and 13th pulses when using operating gas *Ne* at pressure $p_{Ne} = 3.5$ Torr. In the time interval of 0–200 ns, both capacitances, C_{pre} and C_2, are charged. After 200 ns, the ionization pulse discharge develops, which is

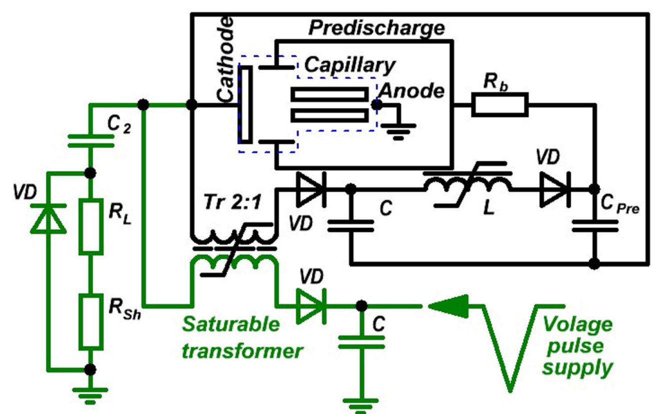

FIG. 2. Auto-synchronized pre-discharge ignition circuit.

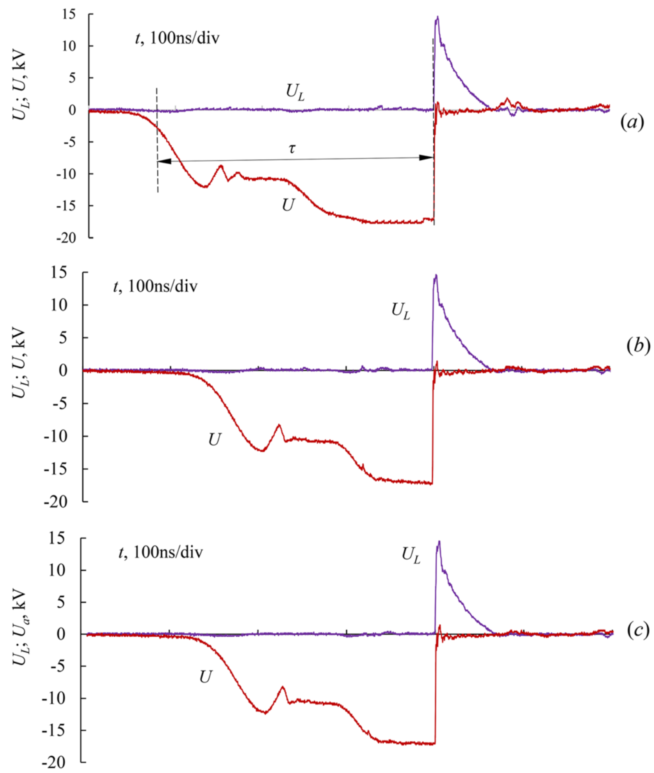

FIG. 3. Waveforms of the voltage on the eptron U and the load U_L for the 1st (a), 2nd (b), and 13th pulses (c). Ne, $p_{Ne} = 3.5$ Torr, $f = 25$ kHz, and $R_L = 200\Omega$.

accompanied by a delay in the voltage rise across capacitance C_1. This is followed by a renewed increase in the voltage across the capacitance, eventually leading to the development of a discharge in the eptron and the generation of voltage across the load. Switching time and efficiency are independent from the initiation method, provided that the initial voltage across the working capacitor C_2 is the same. However, the second initiation circuit variant is distinguished by high stability in the discharge development delay for both the initiating and main pulses. Helium, neon, hydrogen, and their mixtures were used as operating gases. To excite the discharge, the burst length of 20 pulses was used, the burst repetition frequency was 25 Hz, and the repetition frequency of pulses in the burst f varied up to 100 kHz. The quasi-stationary mode of operation was set depending on the amplitude voltage on C_2 by the second or third pulse, as can be seen from the oscillograms in Fig. 3. In the general case for noble gases, the discharge development delay in the second pulse is significantly shorter than in the first one. In the third and subsequent pulses, the delay is statistically equal to the delay in the second pulse. For hydrogen or its mixtures with noble gases, the delay of the second pulse relative to the first one is much less pronounced. Therefore, it can be considered that the quasi-stationary regime for these cases is established starting from the second pulse. All measurements were carried out for the 13th pulse. The voltage on the eptron's anode and load was registered by Ohmic voltage dividers made of low inductive TVO resistors. The current signal was detected using Ohmic shunts with $R_{sh} = 0.1$–$0.5\ \Omega$ made of SMD1225 resistors. The pulse parameters were measured using a Tektronix MDO 3104 oscilloscope, which has a bandwidth of 1 GHz and a sampling rate of 5 GHz..

III. RESULTS OF THE STUDY OF THE INITIAL STAGE OF BREAKDOWN

A. Verification of two-stage switching by eptron

In a wide range of operating voltages from the minimum anode voltage $U = 5$ kV up to $U = 30$ kV, composition and pressure of the operating gas, and similar switching characteristics are registered. Voltage oscillograms on the eptron U and on the load U_L ($R_L = 100\ \Omega$) without initiating pulse and with initiating pulse are shown for the cell with *SiC* cathode at pulse repetition frequency $f = 15$ kHz and hydrogen pressure $p_{H2} = 1$ Torr, Figs. 4(a) and 4(b). Figure 4(a) clearly demonstrates the two-stage breakdown mode with the voltage development time (at the level of 0.1–0.9) at the first stage, $\tau_1 \approx 1$ ns, and at the second stage, $\tau_2 \approx 1.5$ ns. The total voltage rise time due to the gap between the stages is $\tau \approx 7$ ns. Applying the initiating discharge with ballast resistance $R_b = 0$ in the discharge preionization circuit reduces this time to $\tau \sim 2.7$ ns, and in contrast to the mode without preionization discharge, the main part of the voltage on the load, up to $\sim$70%, is realized at the first stage, Fig. 4(b). For the cell with a stainless-steel cathode, Fig. 4(c), or at an increased energy of preionization pulse ($U_{Cpre} = 10$ kV) for the cell with a *SiC* cathode, Fig. 4(d), both stages merge into one with a voltage rise time on the load $\tau \sim 1.5$ ns. The application of a ballast resistor in the preionization circuit separates the stages of discharge development, and at $R_b = 200\ \Omega$, results similar to those presented in Fig. 4(a) are realized.

The parameters of the voltage pulse on the eptron and load remain unchanged up to $f \approx 15$ kHz. Increasing the frequency above 15 kHz gradually brings the development stages closer to each other, and at $f > 50$ kHz they merge into a single one. An example of oscillograms at $f = 70$ kHz for a cell with both *SiC* and stainless-steel cathodes is shown in Figs. 4(c) and 4(d). Nevertheless, the different stages are distinguishable: the first one with duration $\tau_1 \sim 1.2$ ns, in which up to $\sim$15% of the voltage is realized, and the second, with duration $\tau_2 \sim 1.5$ ns with a voltage rise rate on the load 4 times faster. Fast voltage fluctuations on the anode and load are observed for all cases when two-stage breakdown is realized after switching. For a cell with a stainless-steel cathode, the stages are indistinguishable, and the switching time is reduced to $\tau \sim 1.5$ ns at $U = 15$ kV with no evidence of oscillations on the oscillograms. At $U > 20$ kV, slight oscillations occur for this case as well.

B. Modeling of the discharge development process

Typically, the breakdown in the high-pressure discharges is associated with the formation of the ionization wave that gradually propagates between electrodes.[15–18] The design feature of the eptron is that it consists of a capillary dielectric channel that extends into a cathode chamber with a much bigger active cross section. Therefore, in contrast to the numerical modeling in Refs. 16 and 17, the processes on the walls of the capillary and in the transition region between the capillary and the cathode chamber should have a significant influence on the breakdown development. To elucidate the origins of the breakdown scenario and current oscillations in the high-voltage plasma device (eptron), the discharge dynamics were studied in numerical simulations.

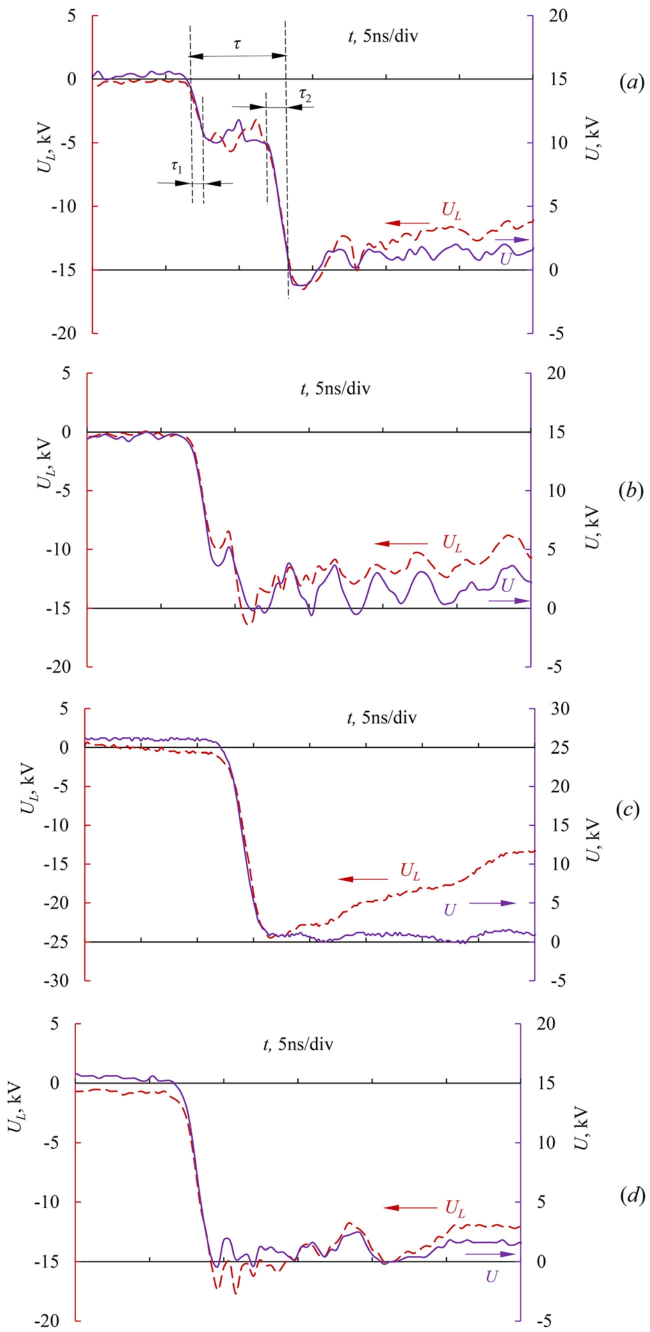

FIG. 4. Voltage oscillograms of the eptron U and the load U_L (a) without preionization discharge and (b)–(d) with preionization discharge. Experimental conditions: Cell with a SiC cathode (a), (b), (d), $R_L = 100\ \Omega$, H_2 at 1 Torr. Cell with a stainless–steel cathode (c), $R_L = 65\ \Omega$, H_2 at 3 Torr. $f = 12.5$ kHz for (a), (b) and 70 kHz for (c), (d).

The fluid model of discharge includes continuity equations for electrons, ions, and mean electron energy U_e,

$$\frac{dn_e}{dt} = \mathrm{div}(\mu_e \mathbf{E} n_e + \nabla(D_e n_e)) + \alpha_i n_e n_g - \beta n_e n_i,$$

$$\frac{dn_i}{dt} = \mathrm{div}(\mu_i \mathbf{E} n_i + \nabla(D_i n_i)) + \alpha_i n_e n_g - \beta n_e n_i,$$

$$\frac{d(n_e U_e)}{dt} = \mathrm{div}(\mu_u \mathbf{E} n_e U_e + \nabla(D_u n_e U_e)) + e\mathbf{E}(\mu_e \mathbf{E} n_e + \nabla(D_e n_e)) - \nu_u n_e n_g,$$

and the Poisson equation for the determination of electric field **E**,

$$\mathrm{div}\nabla\varphi = 4\pi e(n_e - n_i), \quad \mathbf{E} = -\nabla\varphi,$$

where n_e, n_i are electron and ion densities, n_g is the neutral gas density, and e is the elementary charge.

The transport coefficients in the continuity equations for electrons and their mean energy are calculated from the electron energy distribution function (EEDF) $f_e(\varepsilon)$, calculated once for a wide range of electric field magnitudes, in local approximation, when EEDF is supposed to depend only on local electric field magnitude E. The EEDF is found by solving the Boltzmann equation for a given E and neutral gas density. For example,

$$D_e = \frac{1}{n_e}\int \frac{\nu(\varepsilon)}{3n_g\sigma(\varepsilon)} f_e(\varepsilon)d\varepsilon,$$

$$\mu_e = \frac{-e}{n_e}\int \frac{\nu(\varepsilon)}{3n_g\sigma(\varepsilon)} \frac{df_e(\varepsilon)}{d\varepsilon} d\varepsilon,$$

$$D_u = \frac{1}{n_e}\int \frac{\varepsilon\nu(\varepsilon)}{3n_g\sigma(\varepsilon)} f_e(\varepsilon)d\varepsilon,$$

$$\mu_u = \frac{-e}{n_e}\int \frac{\varepsilon\nu(\varepsilon)}{3n_g\sigma(\varepsilon)} \frac{df_e(\varepsilon)}{d\varepsilon} d\varepsilon,$$

where $n_e = \int f_e(\varepsilon)d\varepsilon$, $\nu(\varepsilon)$ is the electron velocity for energy ε, and $\sigma(\varepsilon)$ is the electron transport cross section. The values of D_e, μ_e, D_u, μ_u, α_i, and ν_u are found once before simulation.

For ions, the transport coefficients are taken as

$$\mu_i = \frac{3e}{16 n_g \sigma_i}\left(\frac{\pi}{m_i kT}\right)^{1/2}\left(1 + \frac{9\pi^2 eE}{512 n_g kT\sigma_i}\right)^{-1/2},$$

$$D_i = \mu_i kT,$$

where k is the Boltzmann constant, T is neutral gas temperature, m_i is the ion mass, and σ_i its transport cross section.

For the boundary nodes on the surfaces, an additional sink term is added to the continuity equations,

$$\Gamma_{e,i} = a\mu_{e,i} n_{e,i} E_\perp + \frac{1}{4}\nu_T n_{e,i},$$

where $E_\perp$ is the electric field normal to surface, a is 1 for drift directed to the surface and 0 in the opposite case, ν_T is thermal velocity, depending on energy U_e for electrons, and for ions T_i is taken equal to gas temperature T. In the equation for U_e, the sink term is $\Gamma_e U_e$.

The electrons emitted by the ion bombardment were described by solving the Boltzmann equation for the electron distribution function with the 2D PIC–MCC method. The kinetics of electrons included the elastic collision with background atoms, excitation, and ionization. The Boltzmann equation for emitted electrons was solved self-consistently with the fluid model equations.

The chamber design used in the numerical simulations is shown in Fig. 5(a). The anode, to which a positive potential is applied, is located at the end of the dielectric capillary at $z = 0$. On the opposite side at a distance of 60 mm there is a cathode chamber, the walls of which are at potential $U = 0$. From the outer side, the capillary is partially covered by a conductive screen with $U = 0$.

The study of the discharge ignition dynamics was carried out using a hybrid approach, including hydrodynamic and kinetic descriptions of the plasma. Combined modeling is necessary for correct calculation of the high-energy group of electrons. Since the operating voltages reach tens of kilovolts, the electrons emitted by the ion bombardment of the walls gain significant energy in the cathode sheath. Therefore, the energy of fast electrons is not a local function of the electric field strength E, and their dynamics were modeled *ab initio* by the PIC–MCC method. The system of equations describing the dynamics of the gas discharge included the Boltzmann equation for the distribution function of high energy electrons, the continuity equations for the electron concentration, ion concentrations, and the mean electron energy, and the Poisson equation for the distribution of the electric potential and field strength. The charge on the inner surface of the capillary was calculated by integrating the fluxes of ions and electrons on the wall. The elementary process cross sections for electrons in helium are well known (see, for example, in Refs. 19 and 20).

The ion–electron emission coefficient was varied from $\gamma = 0$ to $\gamma = 0.3$. In numerical simulations, the initial plasma volume concentration in the cathode chamber was varied from $n_{e0} = 10^{11}\ \mathrm{cm}^{-3}$ to $n_{e0} = 3 \times 10^{13}\ \mathrm{cm}^{-3}$, and $n_{e0} = 10^{9}\ \mathrm{cm}^{-3}$ was taken in the capillary. Calculations were performed for the helium gas pressure $p_{\mathrm{He}} = 4$ Torr and the maximum voltage $U = 20$ kV. The anode voltage increased from zero to the peak during 120 ns, Fig. 6(a). As the current increased, the anode voltage dropped according to $U = U_0 - I \times R_L$, where $R_L = 65\ \Omega$.

In the beginning of the discharge ignition, the ionization wave appears near the anode surface inside the dielectric capillary and begins to propagate in the cathode chamber direction. An example of parameter distributions at the time from the beginning of the voltage rise $\Delta t = 80$ ns is shown in Figs. 5(a)–5(d), when the anode voltage is $U = 12$ kV. The concentration of electrons in the cathode cavity is $n_{e0} = 3 \times 10^{11}\ \mathrm{cm}^{-3}$. This case with $n_{e0} = 3 \times 10^{11}\ \mathrm{cm}^{-3}$ refers to the $f = 15$ kHz voltage repetition rate. As seen in Fig. 5, the concentration of electrons at the ionization front reaches $n_e \approx 10^{14}\ \mathrm{cm}^{-3}$ at an

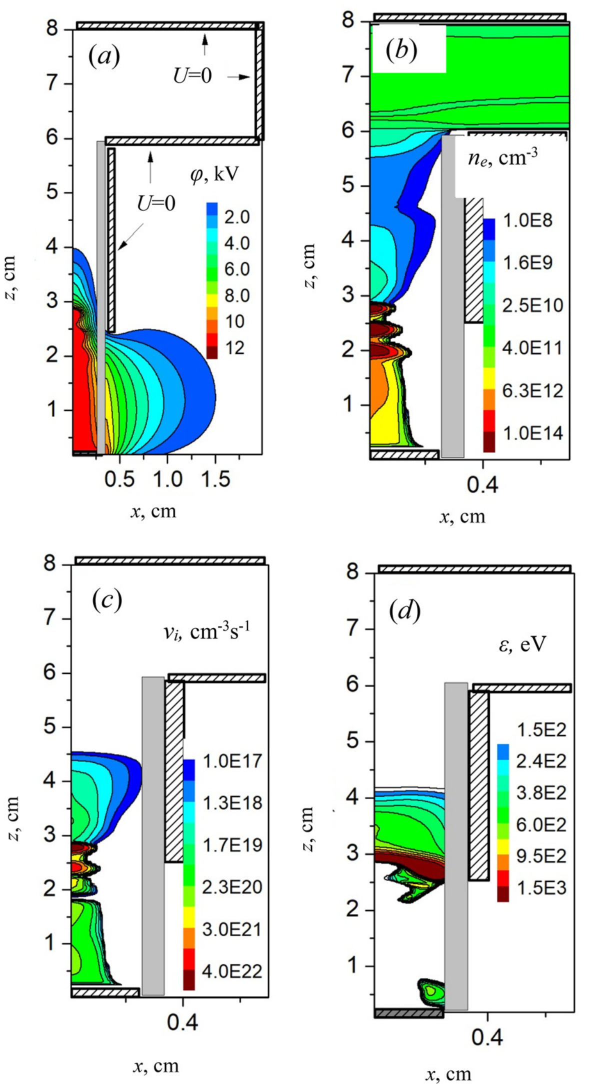

FIG. 5. Spatial distributions of electric potential φ (a), electron concentration n_e (b), ionization rate ν_i (c), and average electron energy ε (d). The concentration of electrons in the cathode cavity $n_{e0} = 3 \times 10^{11}\ \mathrm{cm}^{-3}$.

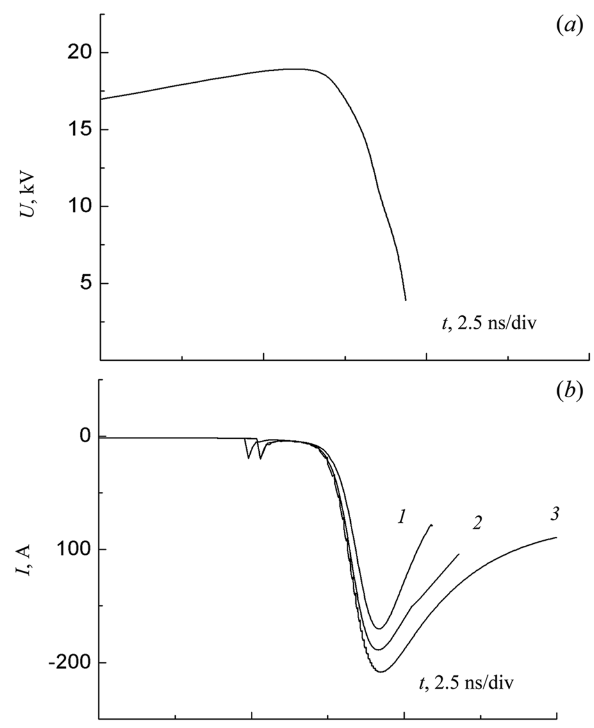

FIG. 6. Temporal distributions of voltage at the eptron U (a) and current through the eptron I (b). He, $p_{\mathrm{He}} = 4$ Torr, $U = 20$ kV. The concentration of electrons in the cathode cavity: $n_{e0} = 3 \times 10^{11}$ (1); 3×10^{12} (2); and 3×10^{13} (3) cm^{-3}.

average electron energy of up to $\varepsilon \sim 1$ keV, which provides an ionization rate $\nu_i \sim 4 \times 10^{22}\,\mathrm{cm^{-3}s^{-1}}$. During the initial phase of the ionization wave propagation in the capillary, the potentials and electron concentrations in both the undisturbed capillary region and cathode chamber remain unchanged. The anode current remains negligible until the ionization front approaches the capillary–cathode junction boundary.

Figure 6(b) shows the time dependence of the current at the anode for different initial plasma concentrations in the cathode chamber. As the plasma concentration increases, the maximum current at the anode increases from $I = 170$ A for $n_{e0} = 10^{11}\,\mathrm{cm^{-3}}$ to $I = 210$ A for $n_{e0} = 3 \times 10^{13}\,\mathrm{cm^{-3}}$. The characteristic time of the current rise is 1–2 ns. The change in the potential distribution on the eptron symmetry axis as the ionization wave propagates in the capillary is shown in Fig. 7.

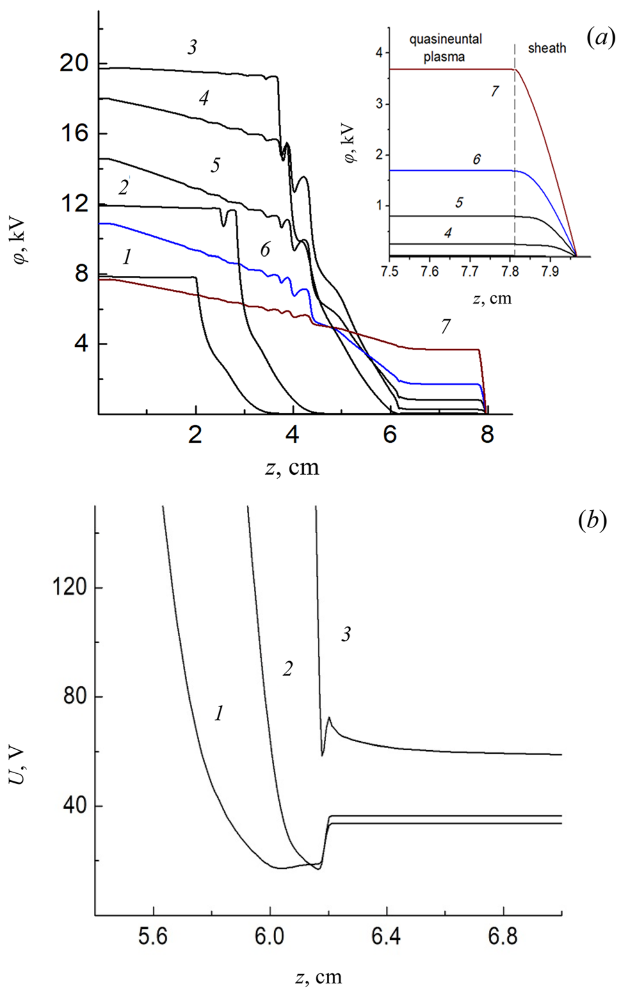

FIG. 7. (a) spatial distribution of potential along the symmetry axis ($r = 0$) at the moments of time: $t = 73.3$ (1); 92.2 (2); 116.3 (3); 117.2 (4); 118.2 (5); 118.5 (6), and 119.1 (7) ns. The inset shows a zoom of the potential distribution near the upper wall of cathode chamber at $z = 8$ cm. (b) Change in the potential well at the capillary–cathode cavity boundary at $t = 115$–116 ns. $t = 0$, it is a moment when the voltage starts to increase from $U = 0$. The concentration of electrons in the cathode cavity $n_{e0} = 3 \times 10^{11}\,\mathrm{cm^{-3}}$.

The ionization front formed near the anode reaches the middle of the capillary with a propagation velocity of $\upsilon_f = z/\Delta t \approx 8 \times 10^7$ cm/s, Fig. 7(a). In self-consistent numerical calculations, the cathode sheath forms near all walls of the chamber. In Fig. 7(a), the sheath near the top of the chamber (at $z = 8$ cm) has 0.18 cm, and the ion density in it is approximately $1.3 \times 10^{11}\,\mathrm{cm^{-3}}$. The virtual cathode, Fig. 7(b), appears near the junction of the capillary and the cathode chamber due to the large difference of the plasma concentration, Fig. 7(b). The sheath of positive ions similar to the cathode sheath forms near the junction due to the much higher mobility of electrons. This potential well separates plasmas in the capillary and the cathode chamber.

As the ionization front approaches the cathode chamber, the virtual cathode disappears, which allows the electrons from the cathode chamber to enter the capillary. The discharge current quickly increases, and the anode voltage drops. The curves 4–7 in Fig. 7(a) show a change in the potential distribution during the current rise. The potential distribution becomes almost linear in the capillary, while the region of quasi-neutrality is preserved in the cathode chamber. In Fig. 8, the spatial distributions of discharge current, ionization rate ν_i, electric potential, and electron concentration are shown at a time when the discharge current has a maximum for $n_{e0} = 3 \times 10^{13}\,\mathrm{cm^{-3}}$.

The spatial distribution of the current and the potential inside the capillary constitutes strong oscillations, Figs. 8(a) and 8(c). The increase in ionization rate and plasma concentration growth are observed inside the cathode chamber in the contact zone with the capillary, Figs. 8(b) and 8(d). Since the plasma in the cathode chamber remains quasi-neutral, accounting for the secondary electrons' contribution to the current has little effect.

C. Experimental studies of oscillation development

Significant oscillations of current and voltage are observed depending on the experimental conditions during 1–6 ns from the moment of breakdown, Fig. 4. The presence of a series resistance in the discharge circuit stabilizes the operation of volumetric discharges. Therefore, in order to carry out measurements over a wider range of current and time intervals, the eptron characteristics with a short-circuited load were studied.

Figures 9(a)–9(c) present oscillograms of the anode voltage and current through the eptron in the absence of the switch auxiliary preionization discharge. These measurements were taken with the *SiC* cathode cell filled with neon at a pressure $p_{Ne} = 2$ Torr and anode voltages $U = 7.5$, 12.5, and 25 kV, respectively. The development of oscillations is clearly visible and is evident over the entire range of voltages investigated and working mixtures used. When the initiating discharge is switched on, the shape of the oscillograms changes dramatically.

Figure 10(a) shows the oscillogram of the anode voltage U and current through the eptron I at the starting voltage $U_0 = 7.5$ kV "without" and "with" the preionization discharge. Figure 10(b) shows the same characteristics, but at $U_0 = 20$ kV. It can be seen that without preliminary initiation the "low-current" discharge is realized first, the current oscillograms of which, depending on the conditions, can take various forms:

- rapid increase during $\sim$1 ns followed by a several-fold drop after 5–10 ns, Figs. 9(a) and 9(b);
- weakly changing current during $\sim$10 ns followed by a sharp increase, Fig. 10(a);

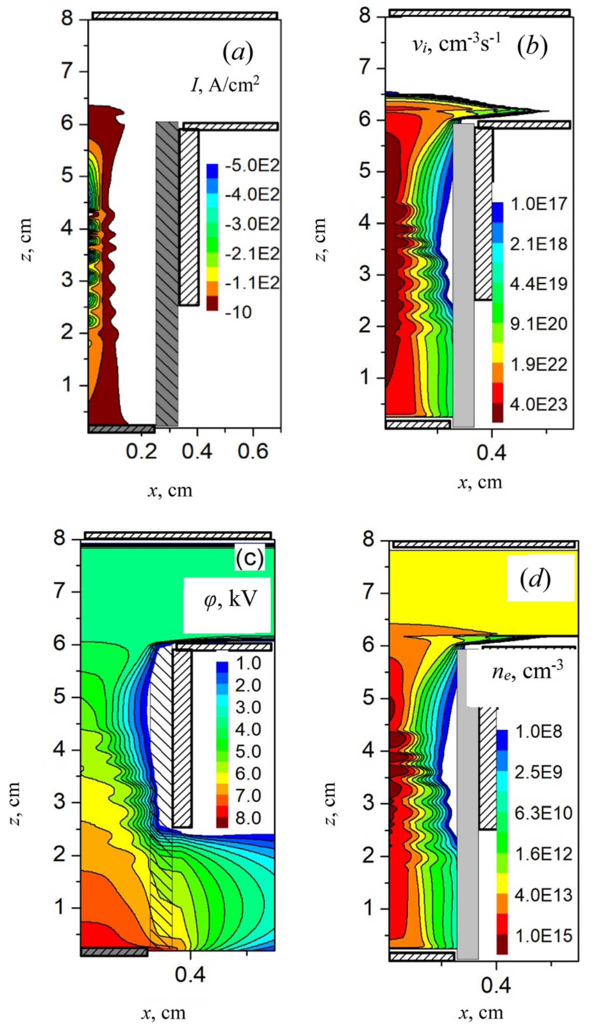

FIG. 8. Spatial distributions of current I (a), ionization rate ν_i (b), electric potential φ (c), and electron concentration n_e (d) at the maximum value of current at the anode. The concentration of electrons in the cathode cavity, $n_{e0} = 3 \times 10^{13}\ \mathrm{cm}^{-3}$.

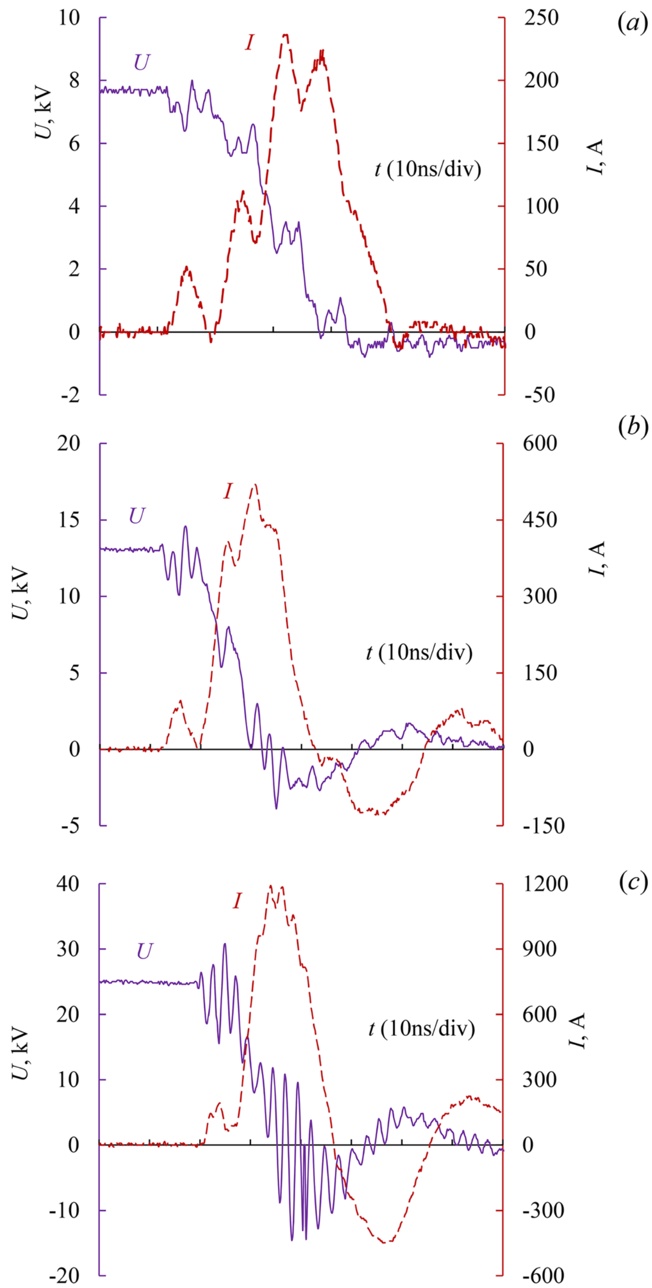

FIG. 9. Oscillograms of anode voltage U and current I without preionization discharge: Ne, $p_{Ne} = 2$ Torr, $f = 10$ kHz.

- relatively slow increase over ∼10 ns followed by a sharp acceleration at high voltages, Fig. 10(b).

The latter is in qualitative agreement with the simulation results, Fig. 8. Voltage oscillograms at this stage always register sharp randomly arranged voltage peaks with a duration of ∼0.5–0.6 ns. It is possible that in reality they are even shorter, since the used oscilloscope has a limited bandwidth.

After the end of the "low-current" stage, a sharp transition to the "high-current" stage with continuing current and voltage fluctuations is always realized. The time between the beginning of these stages decreases with increasing voltage and at $U \approx 20$ kV is equal to 4–5 ns. When the initiating discharge is switched on, the stages become indistinguishable, but at the initial stage the rate of current increase is twice lower than in the subsequent stage. The difference in the oscillograms for eptrons with different cathodes is clearly visible. For the eptron with a *SiC* cathode, in which an order of magnitude lower than the initial electron concentration is realized, the amplitudes of peaks are much higher than in the cell with a stainless steel cathode. For it, current irregularities are almost absent, Figs. 10(a) and 10(b). Increasing the working gas pressure and pulse repetition rate also favors the suppression of oscillations and leads to almost complete stage merging. The current rise rate dI/dt exceeds hundreds of A/ns, and the capillary

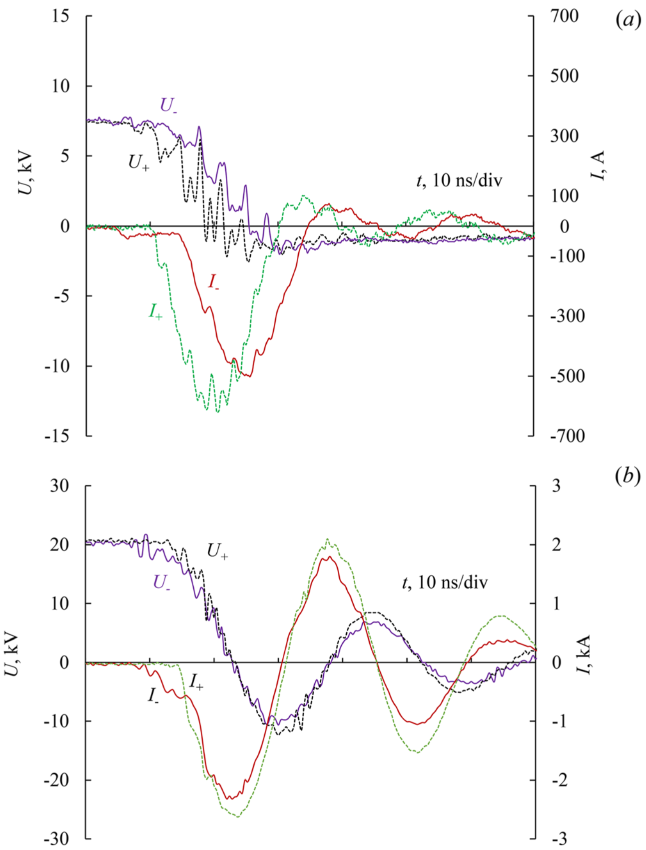

FIG. 10. Oscillograms of anode voltage *U* and current *I* with preionization (U_+, I_+) and without preionization (U_-, I_-) discharge, $R_b = 0.1\ \Omega$: (a) cell with *SiC* cathode. H_2, $p_{H2} = 2$ Torr, $f = 2.5$ kHz; (b) cell with stainless-steel cathode. Ne, $p_{Ne} = 6$ Torr, $f = 10$ kHz.

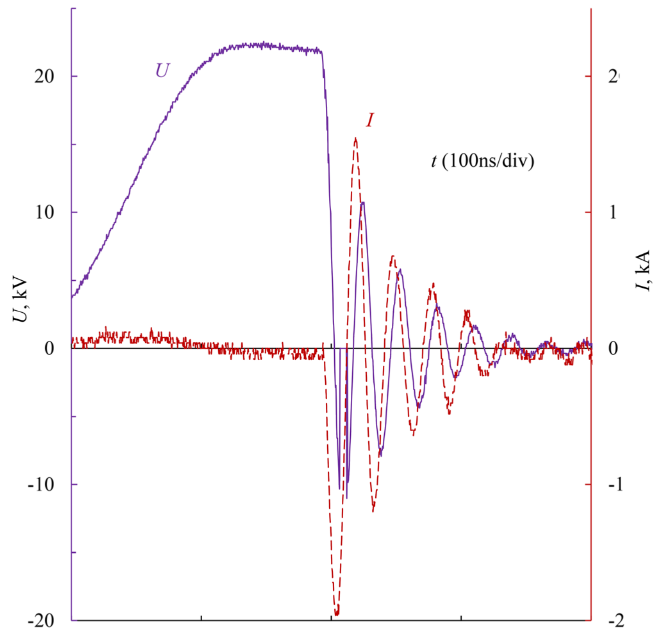

FIG. 11. Oscillograms of anode voltage *U* and current *I* without preionization discharge: Ne, $p_{Ne} = 2$ Torr, $f = 10$ kHz.

plasma retains high conductivity for a long time. Figure 11 shows oscillograms of voltage and current oscillations in neon, characterizing their attenuation when discharging the working capacitance C_2 through the eptron. According to the known formula for the resistance of an oscillating circuit, $R = 2T_0^2/4\pi^2 C\tau_e$ (T_0, oscillation period; τ_e, time of amplitude decrease in "*e*" times), the active resistance of the eptron, R_e, can be calculated. For the given conditions $U_0 = 18.5$ kV and $p_{Ne} = 2$ Torr, resistance is as low as $R_e = 2\ \Omega$. For hydrogen and helium and similar conditions, R_e is larger by ∼40% and 70%, respectively.

In Figs. 12(a)–12(c), the voltage dependences of the current amplitude through the eptron in the first peak, its rise rate *dI/dt*, and the value of the parameter (*dI/dt*)/*U* in hydrogen H_2 for different pressures are shown for the stainless-steel cathode. Accordingly, similar parameters are given for Ne [Figs. 13(a)–13(c)], He [Figs. 14(a)–14(c)], the Ne + H_2 mixture [Figs. 15(a)–15(c)], and the He + H_2 mixture [Figs. 16(a)–16(c)] at different component ratios. It can be seen from these data that the highest current growth rates are realized in the He + H_2 mixture and reach $dI/dt \approx 700$ A/ns. It is interesting to note that the rate of current development grows faster than the initial voltage. Hence, we can conclude that the presence of a finite inductance (∼50 nH) in this realization of the discharge circuit does not limit the rate of current growth, and the achieved value of *dI/dt* is not limiting.

D. Eptron switching time and discussion of the results

According to Ref. 11, the estimated eptron switching time τ_{sc} (by level 0.2–0.8) can be calculated by the equation $\tau_s = ln4/(\alpha\, \upsilon_d\, p)$, where α is the electron multiplication factor, υ_d is the electron drift velocity, and *p* is the gas pressure. In terms of its physical nature, the switching time is the time of rapid current rise, formed after the ionization wave passes through the discharge gap at the final stage of discharge development. In the experiment, this period corresponds to the first stage of breakdown, Figs. 4(a) and 4(b). At large load resistance $R_L > 3$ kΩ, it is close to the time calculated by the formula for τ_s with an accuracy up to ∼20%, and at such values of R_L, the second stage of breakdown is not observed. The appearance of two stages of breakdown occurs at $R_L < 1$ kΩ and at $R_L \leq 100\ \Omega$, as in Fig. 4(a), where it is pronounced. In order to eliminate the reflection of the ionization wave from the cathode cavity and maintain continuity of the current in the discharge circuit, the plasma in the cavity must have appropriate conductivity. For example, at $R_L \approx 100\ \Omega$ and $U = 20$ kV and electric field strength at the capillary outlet $E/N = 10^{-14}$ V × cm^2 ($E = 2$ kV/cm at $p_{He} = 6$ Torr), the required current $I \approx 200$ A is provided according to the equation $I = e\, n_e\, S\, \upsilon_d$ at $n_e \approx 4.5 \times 10^{13}$ cm^{-3} (*S* is the capillary cross section), which is observed experimentally. The same level of n_e is required in the first 0.5–1 ns, when the cathode cavity electron multiplication has not yet become their main supplier. In hydrogen, at $E/N = 10^{-14}$ V × cm^2, the drift velocity $\upsilon_d \approx 1.2 \times 10^8$ cm/s is 1.6 times smaller compared to $\upsilon_d \approx 1.9 \times 10^8$ cm/s in helium, and, therefore, at the preionization pulse energy used, a single-stage breakdown does not

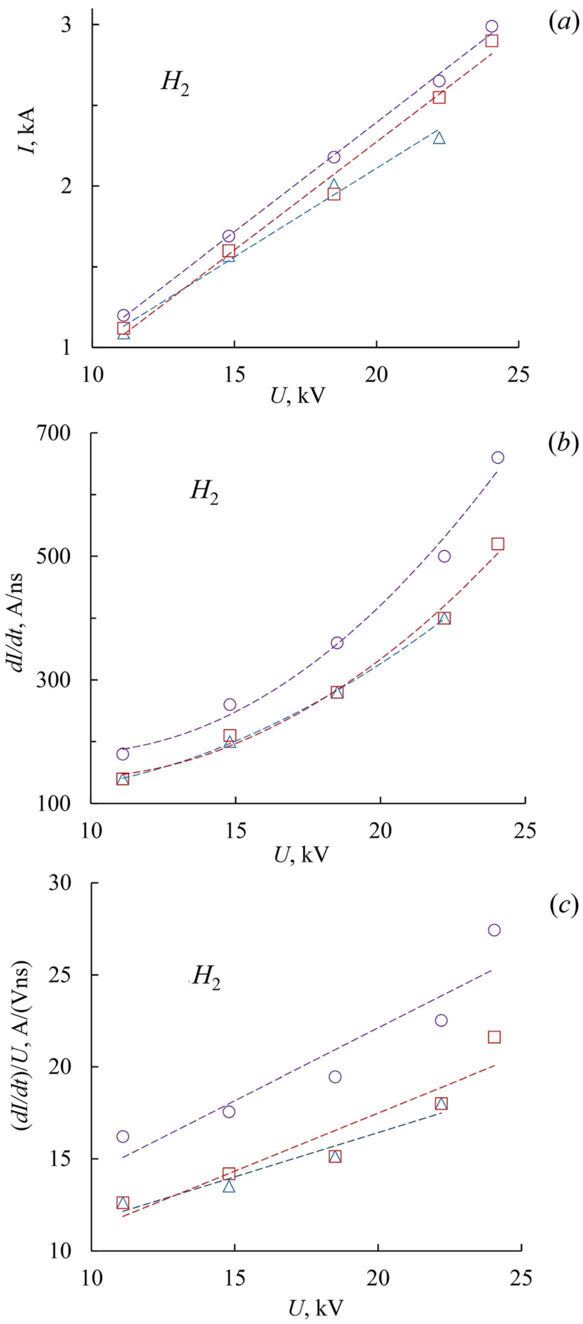

FIG. 12. Dependencies on anode voltage U: current I (a); current rise rate dI/dt (b); parameter $(dI/dt)/U$ (c): H_2, $p_{H2} = 1.7(\Delta)$; $2.2(\square)$; and $3(\circ)$ Torr, $f = 10$ kHz, cell with stainless-steel cathode.

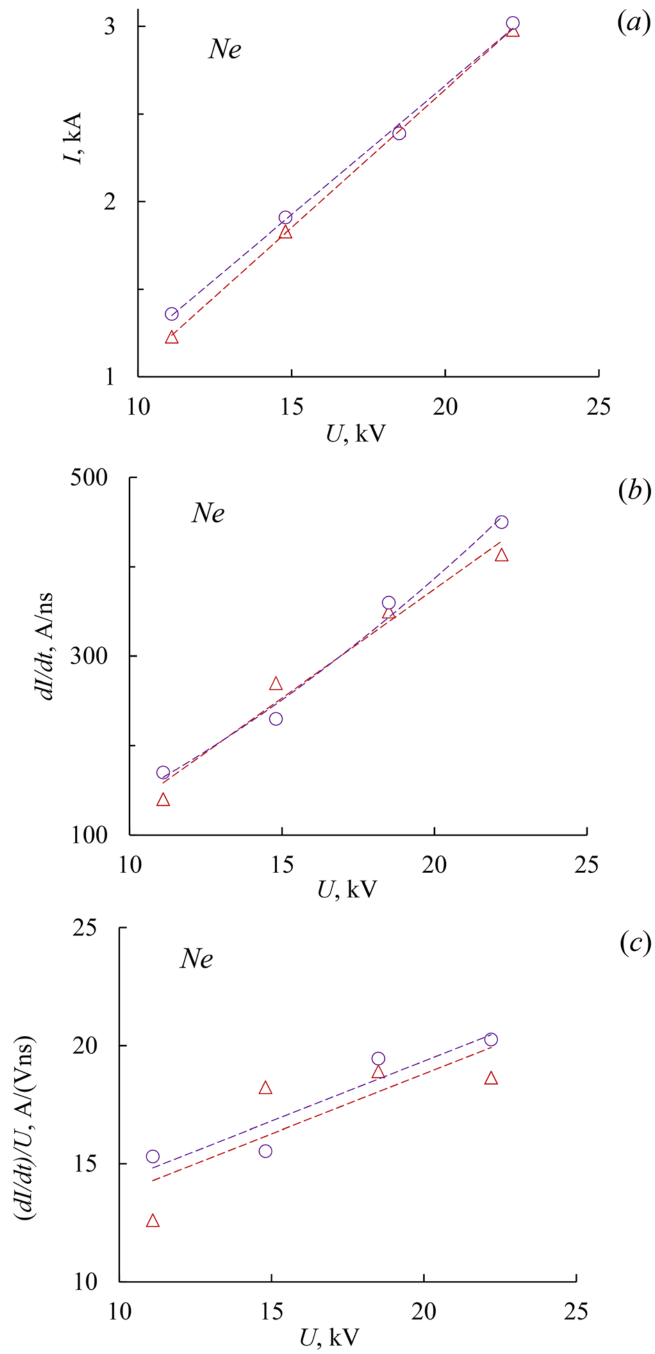

FIG. 13. Dependencies on anode voltage U: current I (a); current rise rate dI/dt (b); parameter $(dI/dt)/U$ (c): Ne, $p_{Ne} = 1.7(\Delta)$ and $3(\circ)$ Torr, $f = 5$ kHz, cell with stainless-steel cathode.

occur. This is achieved only at a high pulse repetition rate due to incomplete recombination of the plasma in the inter-pulse interval.

At elevated hydrogen, $p_{H2} > 2$ Torr, and helium, $p_{He} > 10$ Torr, pressures, the current rise time at the first peak decreases, but due to the decrease in drift velocity, a higher energy of the preionization pulse is required. Therefore, studies over a wider range of τ_s parameters were performed in an eptron with a stainless-steel cathode providing an initial concentration of $n_{e0} > 10^{14}\,cm^{-3}$. The measurement was carried out in two modes. In the first one no preionization of switching with

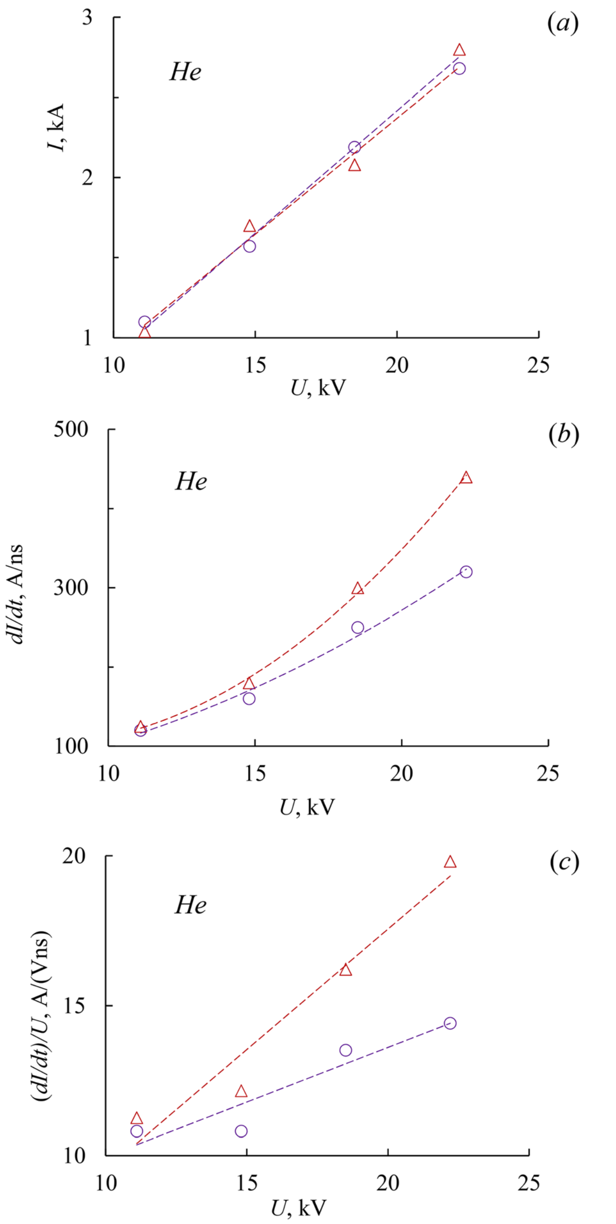

FIG. 14. Dependencies on anode voltage U: current I (a); current rise rate dI/dt (b); parameter $(dI/dt)/U$ (c): He, $p_{He} = 4.5$(○); 6(Δ) Torr, $f = 10$ kHz. Cell with stainless-steel cathode.

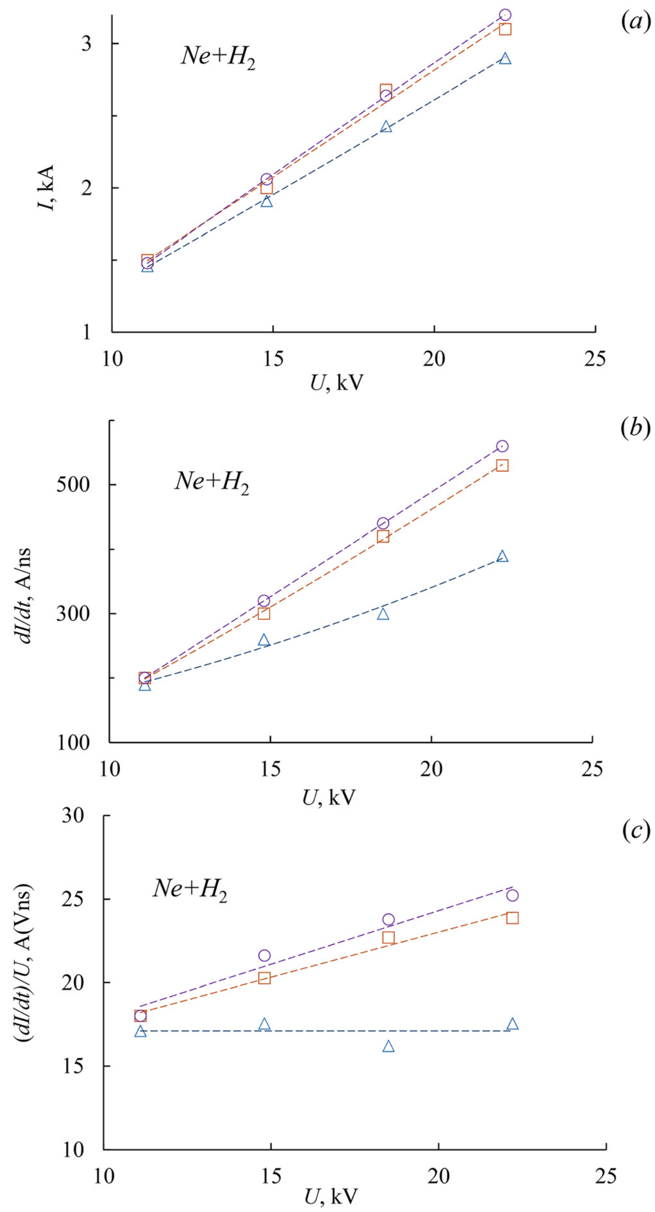

FIG. 15. Dependencies on anode voltage U: current I (a); current rise rate dI/dt (b); parameter $(dI/dt)/U$ (c): Ne + H_2, component ratio 1:1, $p_\Sigma = p_{Ne} + p_{H2} = 1.7$(Δ); 2.3(□), and 3(○) Torr, $f = 10$ kHz. Cell with stainless-steel cathode.

time τ_{sl} was used. In the second mode, under conditions with preionization, complete merging of breakdown stages with switching time τ_{sf} occurred. The time interval of voltage change from a level of 0.2 in the first peak to 0.8 in the second peak was taken as τ_{sl} and τ_{sf}. An example illustrating these measurements is shown in Figs. 17(a) and 17(b) for $p_{H2} = 1.2$ Torr, $U_0 = 22.6$ kV, $f = 100$ kHz, and $R_L = 80\ \Omega$. An important feature useful for practical applications is the much higher switching efficiency in the presence of a preionization discharge. For this case, $U_L/U_0 \approx 0.96$, while without it, $U_L/U_0 \approx 0.85$. The energy spent on preionization of the cathode cavity when equal capacitances are used is $(U_L/U_0)^2 \times 100\% = 5\%$ and decreases to $\sim$2.8% at $U_0 = 30$ kV.

The measurement results demonstrated in Figs. 12–16 allow us to estimate the switching times over a wide range of mixture compositions and operating voltages and to calculate subnanosecond commutation times, assuming that they correspond to the calculated value $\tau_{sc} \sim I/(dI/dt)$, where $I \sim U_0/R_L$. For example, Figs. 18(a) and 18(b) show the dependence of the switching time on the voltage for cases with and without preionization discharge τ_{sf} and τ_{sl}, as well as the

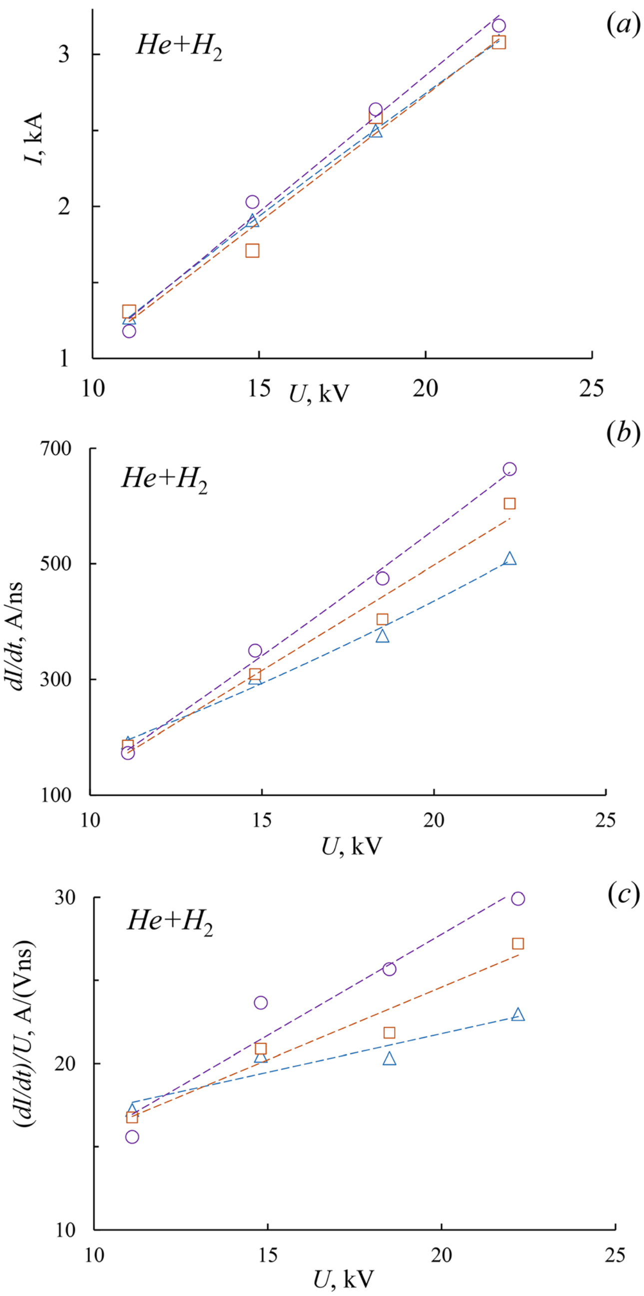

FIG. 16. Dependencies on anode voltage U: current I (a); current rise rate dI/dt (b); parameter $(dI/dt)/U$ (c): He + H_2, component ratio 2:1, $p_\Sigma = p_{He} + p_{H2} = 2(\Delta)$; 4.5(□); and 6(○) Torr, $f = 5$ kHz. Cell with stainless-steel cathode.

parameters τ_{sf}/τ_{sc} and τ_{sl}/τ_{sc} in hydrogen H_2 with $p_{H2} = 3$ Torr and a mixture of Ne + H_2 with pressures of 4 and 2 Torr and $R_L = 80\ \Omega$. It can be seen from the figure that τ_{sf} is several times smaller than τ_{sl}. Nevertheless, the value of τ_{sf} is noticeably larger than the calculated τ_{sc}. The explanation for this, on the one hand, is that the voltage on the eptron decreases during the switching time. On the other hand, at

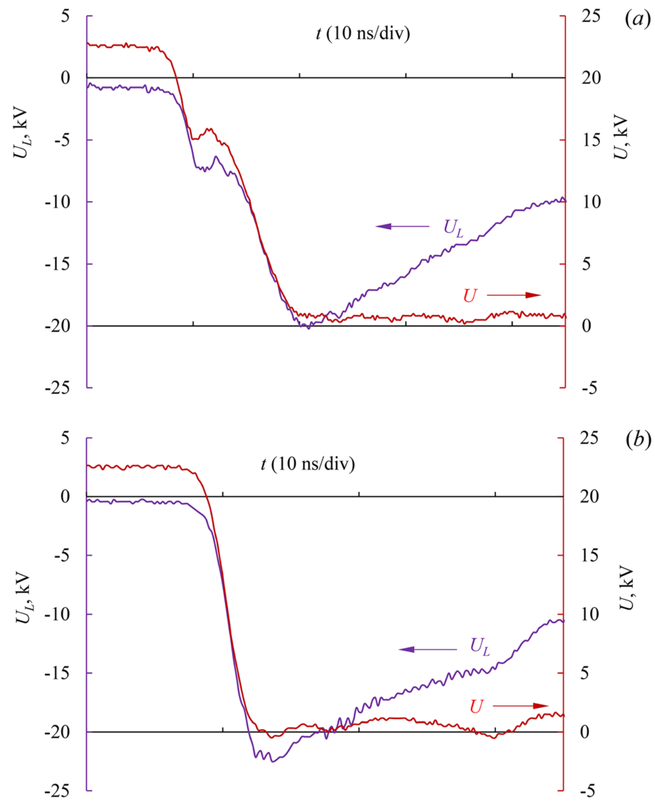

FIG. 17. Oscillograms of voltage at the anode U and load U_L without preionization (a) and with preionization (b) discharge: H_2, $p_{H2} = 1.2$ Torr, $f = 100$ kHz, $R_L = 80\ \Omega$.

$\tau_{sl} < 1$ ns, the switching time measurements are significantly influenced by the insufficient bandwidth of the oscilloscope. This may be the reason for the increase in τ_{sf}/τ_{sc} for $U > 15$ kV.

IV. CONCLUSION

The initial stage of current development in eptron (a device with nano- and subnanosecond switching times based on capillary discharge with a plasma cathode) was investigated. The interest in this class of switches stems from numerous challenges in power electronics, particularly for high-frequency applications (tens to hundreds of kHz) requiring subnanosecond switching of high-voltage pulses (tens of kV).

Experimental results demonstrate that discharge in the eptron typically evolves in two distinct stages, a behavior arising from divergent plasma generation mechanisms in the capillary and the plasma cathode cavity. This difference causes ionization wave reflection during current development, manifesting as observable current and voltage fluctuations during breakdown. By artificially enhancing cathode plasma charge density through increased pulse repetition rates, higher initiating pulse energy inputs, or elevated gas pressure, it is possible to suppress load voltage fluctuations, eliminate the two-stage breakdown characteristic, and achieve subnanosecond duration breakdowns. Simulations reveal the cathode cavity plasma remains quasi-neutral with potential drops below tens of volts, rendering variations in the

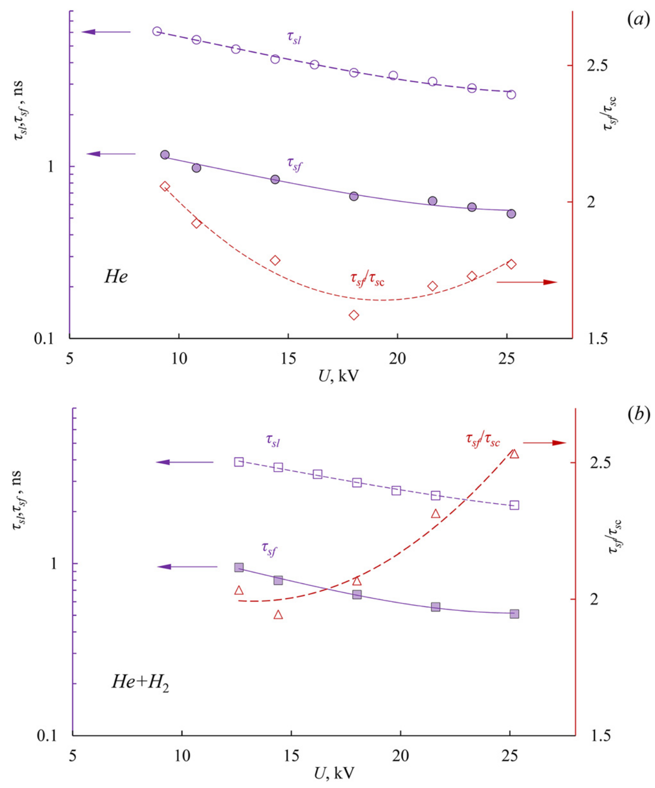

FIG. 18. Dependencies on the anode voltage U: switching time without preionization discharge, τ_{sl}; switching time with preionization discharge, τ_{sf}; parameter, τ_{sf}/τ_{sc}. $f = 30$ kHz. (a) H_2, $p_{H2} = 3$ Torr; (b) He + H_2, $p_\Sigma = p_{He} + p_{H2} = 6$ Torr, component ratio 2:1.

ion–electron emission coefficient $\gamma = 0$–0.3 insignificant for current development. Comparative studies of helium, neon, hydrogen, and their mixtures show the highest current growth rates, $dI/dt \approx 700$ A/ns, occur in He + H_2 mixtures when two-stage switching is eliminated. The observed superlinear increase in dI/dt relative to initial voltage confirms that discharge circuit inductance does not limit current rise rates, indicating the measured dI/dt values do not represent internal switch limitations.

ACKNOWLEDGMENTS

The present work was supported by the Russian Science Foundation, Project No. 24-19-00037 (https://rscf.ru/project/24-19-00037/).

AUTHOR DECLARATIONS

Conflict of Interest

The authors have no conflicts to disclose.

Author Contributions

P. A. Bokhan: Conceptualization (equal); Data curation (equal); Investigation (equal); Methodology (equal); Project administration (equal); Resources (equal); Supervision (equal); Writing – original draft (equal); Writing – review & editing (equal). **P. P. Gugin:** Data curation (equal); Investigation (equal); Methodology (equal). **M. A. Lavrukhin:** Investigation (equal); Methodology (equal); Validation (equal). **D. E. Zakrevsky:** Conceptualization (equal); Investigation (equal); Project administration (equal); Resources (equal); Supervision (equal); Validation (equal); Writing – original draft (equal); Writing – review & editing (equal). **I. V. Schweigert:** Formal analysis (equal); Investigation (equal); Software (equal); Validation (equal).

DATA AVAILABILITY

The data that support the findings of this study are available from the corresponding author upon reasonable request.

REFERENCES

[1]G. A. Mesyats and M. I. Yalandin, "High-power picosecond electronics," Phys.-Usp. **48**, 211–229 (2005).
[2]A. Larsson, "Gas–discharge closing switches and their time jitter," IEEE Trans. Plasma Sci. **40**, 2431–2442 (2012).
[3]L. Li, Z. Zhao, Y. Liu, C. Li, J. Ren, and J. Li, "Repetitive gas–discharge closing switches for pulsed power applications," IEEE Trans. Plasma Sci. **47**, 4237–4249 (2019).
[4]H. Rahaman, J. W. Nam, S. H. Nam, and K. Frank, "Investigation of spark–gap discharge in a regime of very high repetition rate," IEEE Trans. Plasma Sci. **38**, 2752–2757 (2010).
[5]D. M. Goebel, "Cold–cathode, pulsed–power plasma discharge switch," Rev. Sci. Instrum. **67**, 3136–3148 (1996).
[6]B. H. Hamad and A. K. Ahmad, "The effect of intermediate electrode on pseudo-spark switch performance with high repetition rate," Electr. Eng. **104**, 697–703 (2022).
[7]L. M. Merensky, A. F. Kardo–Sysoev, D. Shmilovitz, and A. S. Kesar, "Efficiency study of a 2.2 kV, 1 ns, 1 MHz pulsed power generator based on a drift–step–recovery diode," IEEE Trans. Plasma Sci. **41**, 3138–3142 (2013).
[8]P. A. Ivanov and I. V. Grekhov, "Generation of high–voltage pulses by sharp–recovery SiC drift diodes (n-base versus p-base diodes)," Tech. Phys. **63**, 86–89 (2018).
[9]V. I. Brylevskiy, I. A. Smirnova, N. I. Podolska, Y. A. Zharova, P. B. Rodin, and I. V. Grekhov, "Picosecond–range avalanche switching of bulk semiconductors triggered by steep high–voltage pulses," IEEE Trans. Plasma Sci. **47**, 994–999 (2019).
[10]S. N. Rukin, "Pulsed power technology based on semiconductor opening switches: A review," Rev. Sci. Instrum. **91**, 011501 (2020).
[11]P. A. Bokhan, P. P. Gugin, M. A. Lavrukhin, and D. E. Zakrevsky, "A high-voltage subnanosecond sharpener based on a combination of 'open' and capillary discharges," J. Phys. D: Appl. Phys. **51**, 364001 (2018).
[12]P. A. Bokhan, E. V. Belskaya, P. P. Gugin, M. A. Lavrukhin, D. E. Zakrevsky, and I. V. Schweigert, "Investigation of the characteristics and mechanism of subnanosecond switching of a new type of plasmas switches. II Switching devices based on a combination of 'open' and capillary discharges—eptrons," Plasma Sources Sci. Technol. **29**, 084001 (2020).
[13]P. A. Bokhan, P. P. Gugin, M. A. Lavrukhin, D. E. Zakrevsky, and I. V. Schweigert, "Pulse–periodic gas discharge in atmospheric pressure helium with nanosecond excitation fronts," Phys. Plasmas **30**, 103506 (2023).
[14]M. A. Lavrukhin, P. A. Bokhan, P. P. Gugin, and D. E. Zakrevsky, "100–kHz RM calcium ion NIR laser," Opt. Laser Technol. **170**, 110174 (2024).
[15]L. B. Loeb, "Ionizing waves of potential gradient: Luminous pulses in electrical breakdown, with velocities a third that of light, have a common basis," Science **148**, 1417–1426 (1965).
[16]L. M. Vasilyak, S. V. Kostyuchenko, N. N. Kudryavtsev, and I. V. Filyugin, "Fast ionisation waves under electrical breakdown conditions," Phys.-Usp. **37**, 247–268 (1994).

[17]L. P. Babich, *High–Energy Phenomena in Electric Discharges in Dense Gases: Theory, Experiment and Natural Phenomena* (Futurepast Inc., 2003).
[18]V. F. Tarasenko and S. I. Yakovlenko, "The electron runaway mechanism in dense gases and the production of high–power subnanosecond electron beams," Phys.-Usp. **47**, 887–905 (2004).
[19]I. V. Schweigert, A. L. Alexandrov, D. E. Zakrevsky, and P. A. Bokhan, "Mechanism of formation of subnanosecond current front in high–voltage pulse open discharge," Phys. Rev. E **90**, 051101 (2014).
[20]I. V. Schweigert, A. L. Alexandrov, P. A. Bokhan, and D. E. Zakrevsky, "Breakdown development in helium in high voltage open discharge with subnanosecond current front," Plasma Sources Sci. Technol. **24**, 044005 (2015).